Magnetic evidence for an extended hydrogen exosphere at Mercury

D. Schmid[1], H. Lammer[1], F. Plaschke[2], A. Vorburger[3], N. V. Erkaev[4], P. Wurz[3], Y. Narita[1], M. Volwerk[1], W. Baumjohann[1], and B. J. Anderson[5]

[1]Space Research Institute, Austrian Academy of Sciences, Schmiedlstraße 6, 8042 Graz, Austria
[2]IGEP, Technische Universität Braunschweig, Braunschweig, Germany
[3]Physics Institute, University of Bern, Bern, Switzerland
[4]Institute of Computational Modelling SB RAS, Krasnoyarsk, Russian Federation
[5]The Johns Hopkins University Applied Physics Laboratory, Laurel, Maryland, USA

Corresponding author: D. Schmid, `Daniel.Schmid@oeaw.ac.at`

Abstract

Remote observations by the Mariner10 and MESSENGER spacecraft have shown the existence of hydrogen in the exosphere of Mercury. However, to date the hydrogen number densities could only be estimated indirectly from exospheric models, based on the remotely observed Lyman-α radiances for atomic H, and the detection threshold of the Mariner10 occultation experiment for molecular H_2. Here we show the first on-site determined altitude-density profile of atomic H, derived from in-situ magnetic field observations by MESSENGER. The results reveal an extended H exosphere with densities that are $\sim 1-2$ orders of magnitude larger than previously predicted. Using an exospheric model that reproduces the H altitude-density profile, allows us to constrain the so far unknown H_2 density at the surface which is $\sim 2-3$ orders of magnitude smaller than previously assumed. These findings demonstrate the importance (1) of dissociation processes in Mercury's exosphere and (2) of in-situ measurements giving complementary evidence of processes to remote observations, that will be realized in the near future by the BepiColombo mission.

Index terms: 6235; 0328; 5421; 7837; 7823

Keywords: Mercury; pick-up ion cyclotron waves; hydrogen exosphere; hydrogen surface density

1 Plain language summary

Mercury has an exosphere that contains a variety of species. So far, only two spacecraft have probed the space environment around Mercury: Mariner 10 in 1974, and MESSENGER four decades later. Optical-observations found that Mercury has an abundance of hydrogen in the exosphere. To date no in-situ measurements of hydrogen are available to determine its exact number density: exospheric models that used the optical observations as constrains could only estimate it. For the first time we derive an in-situ density H profile from magnetic field measurements of MESSENGER. From the observations of so-called pick-up ion cyclotron waves in the magnetic field data, it is possible to derive the local H number density, necessary to excite these waves. The results reveal an extended atomic H exosphere with densities decreasing from $\sim 100-10\,\mathrm{cm}^{-3}$ between $2400-15000\,\mathrm{km}$ above the surface. The unexpected large H densities can only be explained by dissociation processes of H_2 molecules. Here we introduce an exospheric model that includes such dissociation processes, which led us for the first time also constrain the H_2 number density. The results suggests that atomic H has additional sinks near the surface, most likely through chemical reactions with OH and O, and that the photochemistry of H_2O in general play an important role for Mercury's exospheric composition.

2 Introduction

Mercury, the innermost planet of our solar system, is surrounded by a tenuous exosphere containing a variety of species that originate from the solar wind, micrometeoroids and the planetary surface. Atomic hydrogen was one of the first exospheric species detected by the Mariner 10 spacecraft in 1974, based on Lyman-α emissions (Broadfoot et al., 1974). Four decades later the detection of the hydrogen exosphere was confirmed by Ultraviolet Visible Spectrometer (UVVS (McClintock et al., 2007)) observations of the MErcury Surface, Space ENvironment, GEophysics and Ranging (MESSENGER (Solomon et al., 2007)) spacecraft (Vervack et al., 2009, 2010, 2016). The measured radiances are related to the total number of Lyman-α photons emitted along the line-of-sight, to obtain the respective column density of the emitting hydrogen. By taking different lines-of-sight, it is possible to determine the exospheric hydrogen column density as a function of altitude. However, to obtain hydrogen number density profiles the measured column densities need to be compared with the output of exospheric models (Chamberlain, 1963; Bishop and Chamberlain, 1989; Wurz and Lammer, 2003; Killen et al., 2007; Mura et al., 2007; Wurz et al., 2010, 2019; Jones et al., 2020). Early models that are fitted to the measured hydrogen radiances yield maximum atomic (H) and molecular (H_2) hydrogen densities near Mercury's surface of $< 1000\,\mathrm{cm}^{-3}$ and $< 2 \times 10^6\,\mathrm{cm}^{-3}$, respectively (Kumar, 1976). Later studies derived $1-2$ orders of magnitude lower H surface densities (Hunten et al., 1988; Vervack et al., 2009) and, based on the detection threshold of the Mariner 10 occultation experiment (Boradfoot et al., 1976), an upper limit of the H_2 surface density of $\leq 1.4 \times 10^7\,\mathrm{cm}^{-3}$ (Hunten et al., 1988; Killen and Ip, 1999).

To date, however, the neutral hydrogen exosphere has been measured only on basis of remote optical detections. In this study we determine for the first time the local H density profile from in-situ (magnetic field) observations. We survey the magnetic field data of MESSENGER in the solar wind for so called ion cyclotron waves (ICWs) which were specifically generated by freshly ionized H atoms. As the neutral H atoms from Mercury's exosphere become photoionized they start to gyrate around the background magnetic field (IMF) and get picked-up by the solar wind. Since the velocity of the new born planetary protons (couple of km/s) is very different from the solar wind velocity (hundreds of km/s), the solar wind plasma becomes unstable to different plasma waves via resonant and non-resonant instabilities (Gary et al., 1991). As has already been shown at Mars and Venus, and since recently also at Mercury, most prominently ICWs are excited by this instability (Mazelle et al., 2004; Russell, 2006; Delva et al., 2008; Schmid et al., 2021). Figure 1 shows a schematic illustration of the ICWs generation mechanism. ICWs are transverse electromagnetic waves near the proton cyclotron frequency. They propagate nearly parallel to the background magnetic field and are either left- or right-hand elliptically polarized: Theory suggests that left-hand polarized waves are produced by a perpendicular pick-up geometry (background magnetic field perpendicular to the plasma flow). Right-hand polarized waves are produced by a parallel pick-up geometry (background magnetic field parallel to the plasma flow) (Wu and Davidson, 1972; Wu et al., 1973). In the solar wind mainly parallel pick-up takes place, due to the small angle between the interplanetary magnetic field and the solar wind streaming direction which is typically $\sim 30°$ (James et al., 2017; Schmid et al., 2021). The right-hand polarized waves propagate in sunward direction with a phase speed on the order of the Alfvén velocity ($v_\mathrm{A} = \frac{B}{\sqrt{\mu_0 \rho}}$, with B the magnetic field strength, μ_0 the permeability of free space and ρ the mass density of the charged particles in the plasma). That speed is slower than the solar wind velocity. Hence, the waves are carried in anti-sunward direction over the spacecraft, thereby reversing the right-hand polarization by the anomalous Doppler shift (Mazelle and Neubauer, 1993). Consequently, in the spacecraft frame a left-hand polarization is observed. In that frame, the waves are shown to be always observed at the local ion gyrofrequency, since the new-born exospheric ions have a negligible velocity relative to the spacecraft. This immediately excludes confusion with ion cyclotron waves generated at the bow shock by back-streaming solar wind protons, because those waves will be observed at the spacecraft with frequencies very different from the local proton gyrofrequency due to their large velocity relative to the spacecraft (Delva et al., 2008, 2011).

To identify ICWs that are specifically generated by the pick-up of freshly ionized planetary hydrogen, we search for time intervals with large transverse magnetic field fluctuations, which are left-hand polarized in the spacecraft frame, and close to the local proton gyrofrequency. From the observed wave power of the identified ICWs we are able to derive the local atomic H density, necessary to produce the observed waves and obtain the first in-situ determined altitude density profile of hydrogen around Mercury. Based on the determined H density profile we also introduce an exospheric model that includes hydrogen photochemistry that can explain the origin of the discovered

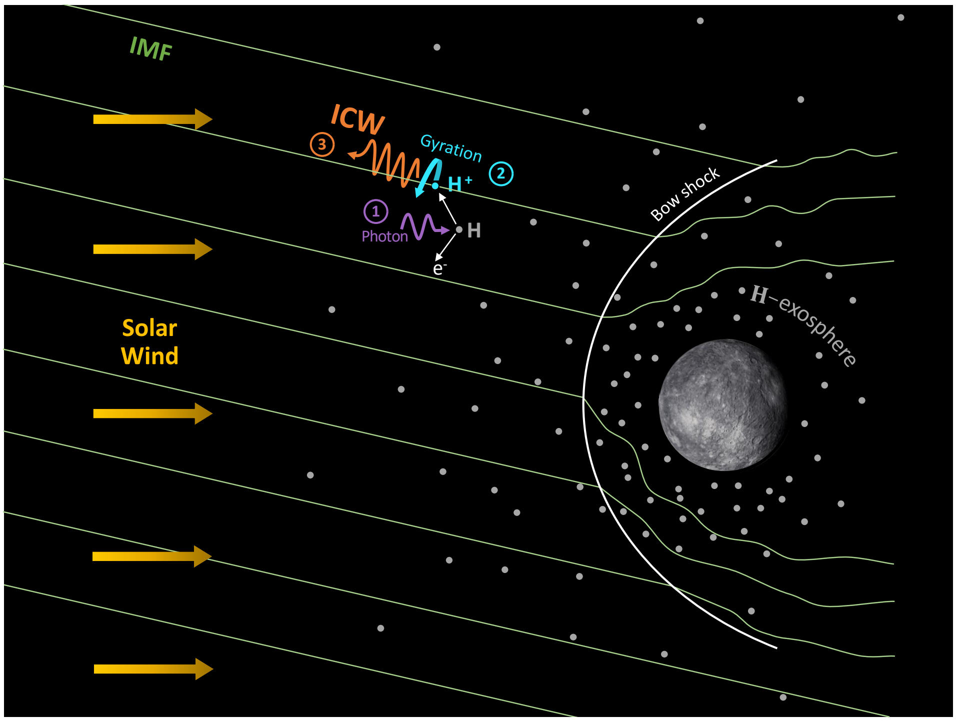

Figure 1. Schematic illustration of the pick-up ion cyclotron generation mechanism. (1) the atomic hydrogen (H, gray dots) get ionized by photons from the sun (purple line); (2) the newborn ions (H^+, blue) start to gyrate around the interplanetary magnetic field (IMF, green lines) and get picked-up; (3) In the solar wind frame of reference the freshly picked-up ions form a secondary distribution in velocity space that is highly unstable to the cyclotron wave instability and ion cyclotron waves (ICWs, orange lines) are excited.

extended atomic H exosphere and which allows us to constrain the so far unknown hydrogen density at the surface.

3 Materials and Methods

Ion cyclotron wave identification criteria

Our starting point is the recently published pick-up ion cyclotron wave (ICW) event list that consists of 5455 events in the space environment around Mercury (Schmid et al., 2021). To identify the pick-up generated ion cyclotron waves, they used the 20 Hz magnetic field observations of MESSENGER (Anderson et al., 2007; Solomon et al., 2007) between March 2011 and April 2015 and applied the following steps to a $\sim 100\,$s long sliding interval:

1. Within each interval the magnetic field data are transformed into a mean-field-aligned (MFA) coordinate system, where the parallel component, $\hat{\mathbf{b}}_{||} = \mathbf{B}_0/|\mathbf{B}_0|$, is given by the average magnetic field, $\mathbf{B}_0 = [B_{\mathrm{x},0}, B_{\mathrm{y},0}, B_{\mathrm{z},0}]$, and the perpendicular components in this coordinate system are chosen to be $\hat{\mathbf{b}}_{\perp 2} = \hat{\mathbf{b}}_{||} \times [0, 0, 1]|$ and $\hat{\mathbf{b}}_{\perp 1} = \hat{\mathbf{b}}_{\perp 2} \times \hat{\mathbf{b}}_{||}$.
2. Each interval (2048 datapoints) is split into 7 sub-intervals of $\sim 30\,$s (512 datapoints) with 50 % overlap. The magnetic field data of each sub-interval are Fourier transformed and the power spectral density matrix is evaluated.

3. The diagonal elements of the matrix give the in-phase power densities, parallel ($P_{||}$) and perpendicular ($P_{\perp} = \frac{1}{2} \cdot (P_{\perp 1} + P_{\perp 2})$) to the mean magnetic field ($\mathbf{B}_0$). The off-diagonal elements of the matrix yield the out-of-phase cross powers, i.e., the field rotation sense around the mean field. The complex off-diagonal elements of the spectral matrix are used to determine the ellipticity and the handedness of the observed wave (Means et al., 1972; Fowler et al., 1967; Arthur et al., 1976; Samson and Olson, 1980). Negative/positive signs refer to left/right-handed polarization of the wave in the spacecraft frame.
4. To evaluate the coherency between the input signals in a particular frequency range and to obtain how stable the components are in phase, the degree of polarization (DOP) of each sub-interval is determined. 100 % indicates a pure state wave and values less than 70 % indicate noise (Samson and Olson, 1980).

The arithmetic means of the obtained power densities and ellipticities of the 7 sub-intervals are calculated. A crucial condition for ion cyclotron waves generated by local ion pick-up is that the observed wave frequency in the spacecraft frame is the same as in the plasma frame (no Doppler-shift) and thus close to the local proton gyrofrequency (Delva et al., 2008). To provide a reliable identification, we calculate the proton gyrofrequency $f_{\mathrm{c,H^+}} = qB_0/(2\pi m)$ and error range $\Delta f_{\mathrm{c,H^+}} = q\sigma_B/(2\pi m)$, with proton mass m, charge q and the average and standard deviation of the magnetic field magnitude B_0 and σ_B, for each $\sim$ 100 s time interval and apply the following criteria in the frequency range $\Delta F = [0.8 \cdot (f_{\mathrm{c,H^+}} - \Delta f_{\mathrm{c,H^+}}), f_{\mathrm{c,H^+}} + \Delta f_{\mathrm{c,H^+}}]$:

- The power density per component is integrated in the frequency range ΔF to account for power maxima just below the calculated gyro frequency. The ratio between the integrated perpendicular $E_{\perp}$ and parallel fluctuations $E_{||}$ is evaluated and needs to be larger than 5: $E_{\perp}/E_{||} > 5$.
- Within ΔF the ellipticity ϵ should be smaller than -0.5, to ensure a left-handed polarization of the observed wave.
- The degree of polarization DOP of all sub-intervals is required to be larger than 0.7 within ΔF, to maintain large coherency of the observed wave and that the signal-to-noise ratio is high.
- The maximum of the perpendicular fluctuating field $P_{\perp}$ is within the limits of ΔF, to ensure that the observed wave is dominated by the ion cyclotron mode.

Figure 2 depicts an example of an identified ion cyclotron wave. Panel S1(a) shows the magnetic field observation in mean-field-aligned (MFA) coordinates. The two perpendicular components (red and blue) are coherent and their fluctuations dominate over the parallel magnetic field variations (green). This can be also seen in Panel S1(b) where the perpendicular component of the power spectral density (red) prevails over the parallel component (green), indicating that the observed wave is rather transverse than compressional around the proton cyclotron frequency $f_{\mathrm{c,H^+}} = 0.43$ Hz (marked as solid black line). The area between the two dashed lines illustrates the integration frequency range ΔF, used to evaluate the power densities, ellipticity and degree of polarization. Panel S1(c) shows the hodogram in each plane of the MFA coordinate system for the time interval from Panel S1(a). The observed wave is almost circularly left-hand polarized with an estimated ellipticity of ~ -0.70.

For this study only those time intervals when MESSENGER was located in the solar wind are preselected. Utilizing an extended boundary dataset (Winslow et al., 2013; Philpott et al., 2020), 3969 (of 5455) time intervals were allocated in the solar wind.

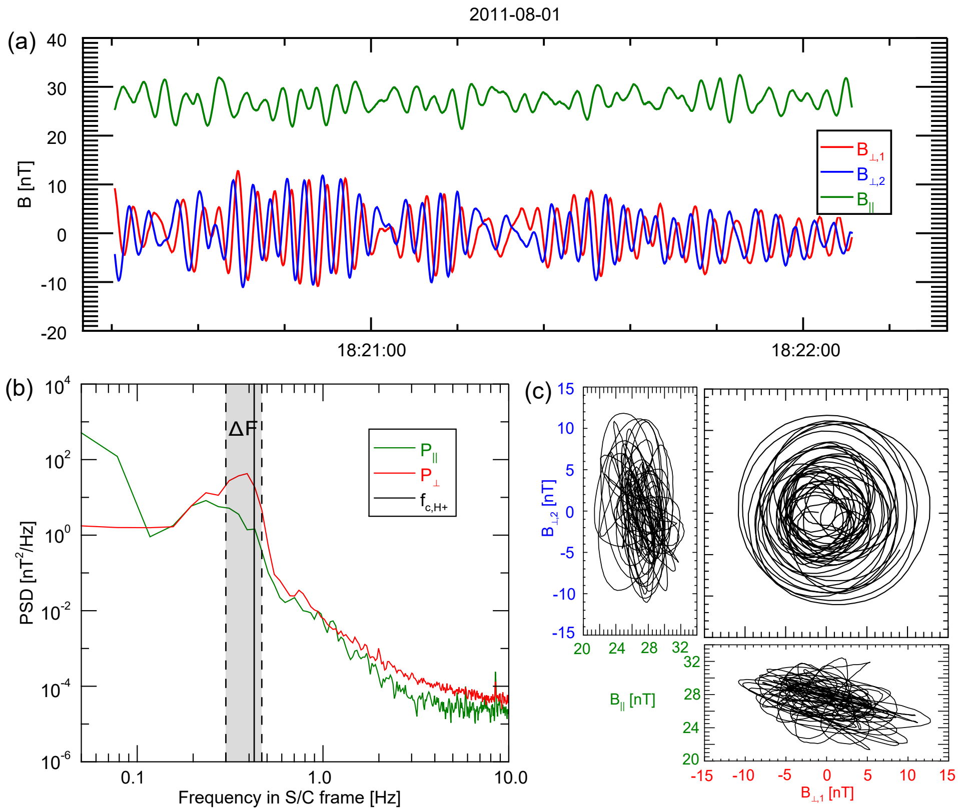

Figure 2. Example of an identified ion cyclotron wave (ICW). Panel (a) shows the magnetic field observations in mean-field-aligned (MFA) coordinates, panel (b) the power spectrum, and panel (c) hodograms of the perpendicular and parallel magnetic field components.

Injection velocity estimate

Due to the limitation of the plasma measurements of MESSENGER, we use a solar wind propagation model (Tao et al., 2005) (provided by the AMDA database) that was successfully applied for Mercury (Schmid et al., 2021) to get an approximate estimate of the plasma density $n_{\rm SW}$ and velocity $V_{\rm SW}$ of the solar wind during the ICW observation period. As the injection velocity ($\mathbf{V}_{\rm inj}$) we use the aberrated solar velocity ($\mathbf{V}_{\rm SW}$), modified by the orbital motion of Mercury ($\mathbf{V}_{\rm Mercury}$) as provided by the Navigation and Ancillary Information Facility (NAIF, (Acton, 1996)) $\mathbf{V}_{\rm inj} = -\mathbf{V}_{\rm SW} + \mathbf{V}_{\rm Mercury}$. The injection velocity vector is also used to determine the solar zenith angle (SZA), which is used to select events dayside of the terminator (SZA $<$ 90°), to maintain that the observed waves are freshly generated from local ion pick-up and to omit waves that might already diminish (Delva et al., 2009). From the 3969 preselected time intervals, 2247 pertain to observations dayside of the terminator. These 2247 ICWs finally constitute the dataset for this study.

4 Results

Based on an automatic search algorithm, with specific selection criteria for ICWs generated by the pick-up of planetary protons, we identify 2247 ICWs during 4 years of MESSENGER solar wind observations upstream of the Mercury terminator (Schmid et al., 2021). These 2247 ICWs yield the basis for this study.

ICWs should be generated locally through initial ionization of the neutral atomic H. To test this, we transform the observation locations into electromagnetic coordinates to examine possible asymmetries with respect to the convection electric field. ICWs propagate with speeds that are on the order of (or lower than) the local Alfvén velocity ($V_{\rm A}$), which should be much lower than the injection speed ($V_{\rm inj}$) (Delva et al., 2009). Thus, we also evaluate the $V_{\rm A}/V_{\rm inj}$ ratios during the ICWs detection. Since the initial velocity of the neutral hydrogen before ionization is negligible in the planetary frame, we assume that the injection velocity of the new-born exospheric ions dirctly corresponds to the aberrated solar wind velocity in the solar wind frame of reference.

Figure 3(a) shows the position of the 2247 ICWs in the local electromagnetic coordinate system: $X_{\rm MBE}$ points sunward, opposite to the aberrated solar wind velocity ($\mathbf{V}_{\rm inj}$), $Y_{\rm MBE}$ is positive in the direction of the background magnetic field ($\mathbf{B}_0$) component, perpendicular to $X_{\rm MBE}$, and the $Z_{\rm MBE}$ axis is positive in the direction of the convection electric field ($\mathbf{E} = \mathbf{V}_{\rm inj} \times \mathbf{B}_0$). There are several indications in Fig. 3(a) that the observed ICWs are generated locally: (1) ICWs occur at large positive $X_{\rm MBE}$, far from the planet, suggesting that the ICWs should have propagated against the solar wind flow with a velocity faster than the solar wind speed, which is very unlikely. (2) ICWs are evenly distributed between $\pm Z_{\rm MBE}$ and since there is no known mechanism to move ions across the magnetic field against the electric field into the negative motional electric field region, the ICWs needed to be generated locally (Delva et al., 2008). Panel (b) depicts the normalized occurrence rate of the estimated $V_{\rm A}/V_{\rm inj}$ ratios. The histogram confirms the second assumption: The Alfvén velocity is significantly smaller than the injection velocity of the new-born exospheric ions into the background (solar wind) plasma. From the results in Fig. 3 we conclude that the underlying assumptions for reliable density estimations are fulfilled.

From the observed wave power of the ICWs we derive the required pick-up proton densities in the same way as previous studies did at Venus (Delva et al., 2009): The total free energy, $E_{\rm free}$, which is required to excite cyclotron waves from a pick-up ion ring-beam distribution is approximately given by (Huddleston and Johnstone, 1992):

$$E_{\rm free} = \frac{1}{4} m_{\rm i} n_{\rm H^+} V_{\rm A} V_{\rm inj} \left[(1+\cos(\alpha))^2 + (1-\cos(\alpha))^2 \right]. \tag{1}$$

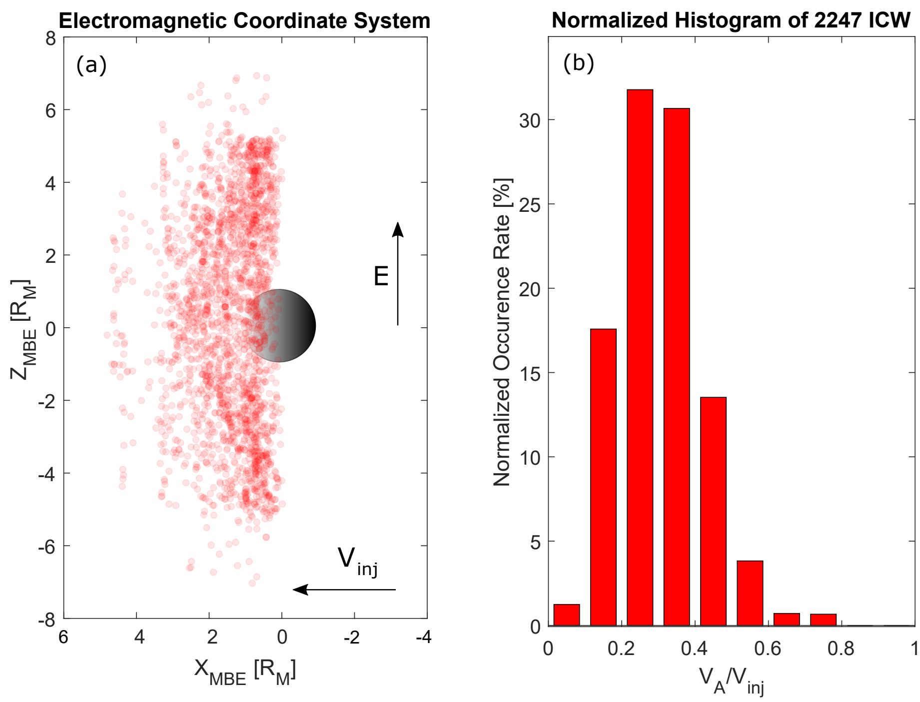

Figure 3. Observationally evidence that the ion cyclotron waves are locally generated from the pick-up of newborn ions. Panel (a) shows the position of the 2247 ion cyclotron waves (ICWs) in electromagnetic coordinates: X_{MBE} points sunward opposite to the injection velocity $\mathbf{V}_{\mathrm{inj}}$, Y_{MBE} is positive in direction of the mean magnetic field $\mathbf{B}_0$ component perpendicular to X_{MBE}, and the Z_{MBE} axis is positive in direction of the convection electric field $\mathbf{E} = \mathbf{V}_{\mathrm{inj}} \times \mathbf{B}_0$. Panel (b) shows the normalized occurrence rate of the ratio between the local Alfvén and injection velocity ($V_{\mathrm{A}}/V_{\mathrm{inj}}$) during the ICW observation.

Here, m_{i} and $n_{\mathrm{H+}}$ are the mass and density of the pick-up ions, V_{A} is the local Alfvén velocity, calculated from the modeled solar wind density and the in-situ magnetic field measurements, V_{inj} is the plasma injection velocity and $\alpha(\mathbf{V}_{\mathrm{inj}}, \mathbf{B}_0)$ is the pitch angle between the plasma injection velocity and background magnetic field. Inverting Eq.1 for $n_{\mathrm{H+}}$ yields the pick-up ion density, under the assumption that the entire free energy of the ring-beam distribution is transfered to the wave and corresponds to the observed ICW energy, $E_{\mathrm{free}} = \int_{\Delta F} P_{\perp} df$ (Delva et al., 2009); $n_{\mathrm{H+}}$ can thus be understood as a lower limit for lower energy transfer rates. Hybrid simulations have shown that the ICWs grow rapidly until a quasi-steady level is reached after $60 - 100$ ion gyrations (Cowee et al., 2012). It should be mentioned that simulations assume specific seed particle distributions which develop in time in an isolated system. Under quasi-stationary conditions that the freshly produced (through photoionization) and lost (to the solar wind) ions are in equilibrium, however, the characteristic time $(2\pi f_{\mathrm{c,H+}} \cdot t)$ of $60 - 100$ ion gyrations until the ICWs fully develop, can be directly applied to an open system as is the case here. Based on the (conservative) assumption that the full energy transfer from the ions to the waves takes 100 gyro periods, the pick-up ion density in this time should be balanced by the ion production rate, which can be estimated by multiplying the neutral hydrogen density n_{H} with the photoionization rate ν:

$$\frac{n_{\mathrm{H}^+} 2\pi f_{\mathrm{H}^+}}{100} = n_{\mathrm{H}} \nu, \tag{2}$$

with n_{H^+} being the estimated pick-up ion density from Eq. 1 and f_{H^+} the gyrofrequency. The photoionization rate varies significantly with the solar activity and the radial distance of Mercury to the Sun. Therefore, we modified the ionization rate according to the Flare Irradiance Spectral Model (FISM-P, (chamberlain et al., 2008)) of Mercury, which reflects the solar activity, and the radial distance of Mercury to the sun during the ICW observations: First we normalized the FISM-P irradiance between $[0, 1]$, where 0 corresponds to $0.028\,\mathrm{Wm^{-2}s^{-1}nm^{-1}}$ and 1 to $0.1\,\mathrm{Wm^{-2}s^{-1}nm^{-1}}$ (which in turn corresponds to the minimum and maximum spectral irradiance index at 121.5 nm during solar cycle 24). Based on the normalized FISM-P irradiance index we interpolate the corresponding photoionization rate at Earth's orbit between minimum $7.26 \times 10^{-8}\,\mathrm{s^{-1}}$ (quiet Sun = 0) and maximum $1.72 \times 10^{-7}\,\mathrm{s^{-1}}$ (active Sun = 1) (Huebner and Mukherjee, 2015). In the last step, we rescale this ionization rate from Earth's orbit (1 AU) to the square of the distance of Mercury during the ICW observation ($0.31 - 0.47$ AU). Figure 4 shows the radial dependence of the estimated H number density. The radial distance is given from the planet's center in Mercury radii ($R_{\mathrm{M}} = 2440\,\mathrm{km}$) (top axis), and from the surface (bottom axis). The blue boxes represent the the median number densities of H and the upper/lower quartiles. The black error bars are the maximum and minimum densities within the $0.5\,R_{\mathrm{M}}$ bins. The obtained medians decrease from $\sim 100\,\mathrm{cm^{-3}}$ to $\sim 10\,\mathrm{cm^{-3}}$ between $2\,R_{\mathrm{M}}$ and $7.5\,R_{\mathrm{M}}$. The relationship is approximately logarithmic between number density and radial distance. Although the number densities from individual ICW events can vary considerably within the bins (see error bars), the differences between the upper and lower quartiles are small.

Interestingly, the obtained H density profile follows the trend of exospheric Monte Carlo models, which have successfully been applied in previous studies (Wurz and Lammer, 2003; Wurz et al., 2010; Pfleger et al., 2015), but are $1-2$ orders of magnitude larger and lie in-between the atomic (H) and molecular (H_2) profiles of these models (see e.g Fig. 3 in (Wurz et al., 2019)). This might indicate that dissociation processes, which have not been included in the models, may play an important role in Mercury's exospheric composition. The dashed green line in Fig. 4 show the result of the H_2 profile that is modeled with a kinetic Monte Carlo model (see Appendix A) for the commonly assumed surface number density of $1.4 \times 10^7\,\mathrm{cm^{-3}}$, given by the upper limits derived from the detection threshold of the Mariner 10 occultation experiment (Hunten et al., 1988; Killen and Ip, 1999). From this H_2 profile we model the corresponding ionization, dissociation and recombination products that result in H_2^+, H^+ and H atoms (details of the model are given in Appendix A). The solid green line shows the resulting H density profile originating from the dissociated H_2 molecules, which are most likely the major source for H atoms at altitudes that are $> 1.5\,R_{\mathrm{M}}$. Although the modeled density profile reproduces the trend of the altitude H density profile obtained from the in-situ ICW observations, the modeled densities are still higher, indicating that the H_2 surface density should be lower than $\sim 1.4 \times 10^7\,\mathrm{cm^{-3}}$. The best results that reproduce the inferred H densities from the ICW observations are obtained for a H_2 surface density of $\sim 8 \times 10^4\,\mathrm{cm^{-3}}$ (dashed red line). The red lines correspond to the H_2 and H profiles based on this lower H_2 surface density which is $\sim 2 - 3$ orders of magnitude lower than the previously assumed surface density of $\leq 1.4 \times 10^7\,\mathrm{cm^{-3}}$.

5 Conclusions and discussion

So far, only remote measurements of hydrogen Lyman-α emissions have been used to evaluate the hydrogen exosphere at Mercury. In this study we present for the first time the number density profile of hydrogen in Mercury's exosphere, based on in-

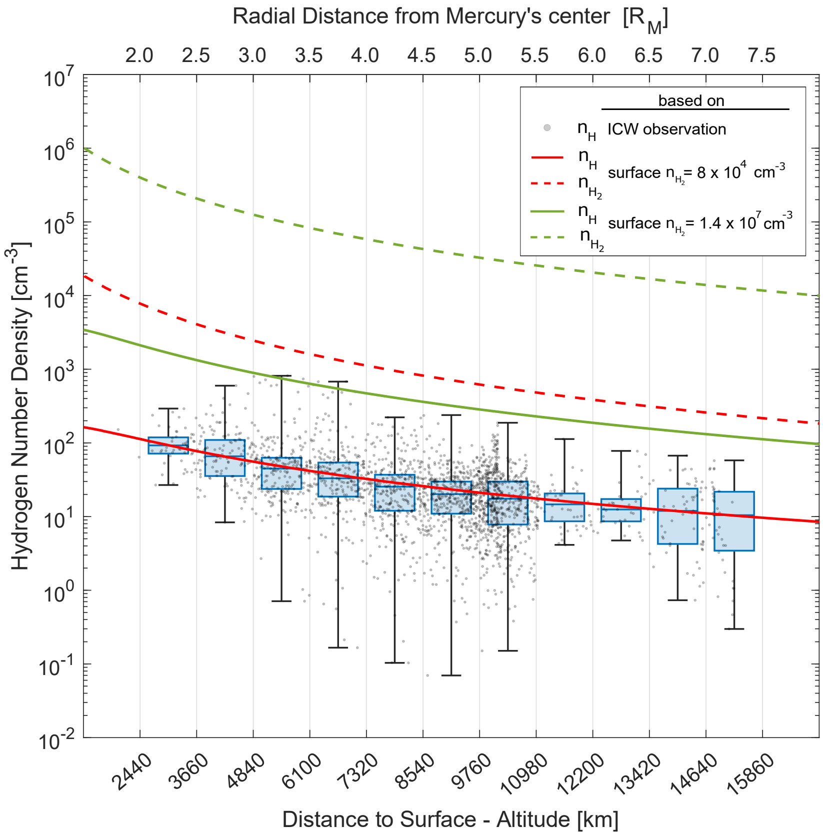

Figure 4. Altitude density profile of hydrogen around Mercury. Boxplot of the estimated hydrogen densities as a function of the radial observation distance. The black error bar indicate the minimum and maximum number density within each 0.5 R_M bin. The boxes indicate the lower and upper quartiles and the horizontal blue lines the median number density of each bin. The gray dots depict the derived hydrogen number densities of the 2247 ICW events. The green and red lines are the simulation results obtained from an exospheric model of atomic H (solid lines) that originate from dissociation of H_2 molecules (dashed lines), based on H_2 surface number densities of $1.4 \times 10^7\,cm^{-3}$ (green lines) and $8 \times 10^4\,cm^{-3}$ (red lines), respectively.

situ magnetic field measurements of ion cyclotron waves (ICWs) by the MESSENGER spacecraft.

For this study we assume that the observed ICW wave energy exactly corresponds to the free energy in the ring-beam distribution of the pick-up ions (Huddleston and Johnstone, 1992). Simulations, however, show that the energy transfer from the ions to the waves might be 3-4 times smaller, because the energy is distributed between wave growth and ion heating (Cowee et al., 2007). Consequently, the number densities obtained in this study might be underestimated. The variability of the energy transfer efficiency might also result in the broad distribution of estimated number densities at similar radial radial distances from Mercury (see black error bars in Fig. 4). However, these simulations only consider a rather perpendicular pick-up geometry with only small parallel relative drift velocities. Due to the small cone angle between the interplanetary magnetic field and solar wind velocity, the ICWs used in this study are rather generated under quasi-parallel pick-up configurations (Schmid et al., 2021). Theoretical studies on the growth rates for parallel and perpendicular pick-up geometries suggest that perpendicular picked-up ions produce ICWs with low growth rates and that parallel picked-up ions generate ICWs with large growth rates (Wu and Davidson, 1972; Wu et al., 1973). Therefore, the observed ICWs are most likely fully developed in less than the assumed 100 ion gyro periods. Together with the assumption that all of the free energy from the pick-up ions is transfered to the ICW the derived H density may thus be understood as a lower limit, but is still larger than predicted by recent exospheric models, which assume a thermal H atom population with dayside H atom surface densities of $23\,\mathrm{cm}^{-3}$ (Hunten et al., 1988; Killen and Ip, 1999).

In order to make an quantitative statement on the reliability of the estimated hydrogen densities in this study, we transform them to Lyman-α radiances and compare them to the previously detected radiances of MESSENGER and Mariner 10. The radiance R is given in rayleighs by $4\pi R = g \cdot N/10^6$, where N is the integrated column density along the line-of-sight in atoms cm^{-2} and g the photon scattering coefficient (referred to as g-value). The g-value for hydrogen at Mercury is 5.3×10^{-3} photons atoms^{-1} s^{-1} (Hunten et al., 1988). When the exosphere of Mercury is viewed externally along the line-of-sight of the spacecraft that is tangent to a spherical shell of radius r (i.e. radial vector form the center of the planet), the column density N at this position can be expressed in terms of the local scale height h and the local density of scattering hydrogen atoms n_{H} with $N = n_{\mathrm{H}} \cdot \sqrt{2\pi \cdot h \cdot r}$ (Chamberlain and Hunten, 1987). h can be directly obtained from Fig. 4 by e-folding of the hydrogen density n_{H} at position r. Based on this simple approach we are able to transform the estimated hydrogen densities n_{H} to their Lyman-α radiances at various altitudes and thus obtain the expected airglow around Mercury. The blue line in Fig. 5 shows the Lyman-α radiances obtained from the median (blue dots), upper and lower quartile (blue errorbar) of the observed hydrogen densities in Fig. 4. The gray and black dots indicate the Lyman-α observations of MESSENGER and Mariner 10 during their flybys (Vervack et al., 2011; Ishak, 2019). Although the hydrogen densities derived from the ICW observations are more than one order of magnitude larger than estimated by previous models, they are still in good agreement with the upper limits of the Lyman-α radiances measured by MESSENGER and Mariner 10, suggesting that the derived densities are in the correct order of magnitude.

A number of exospheric models and computational simulations have been developed to explain these highly complex and interrelated source and loss processes to understand the composition of Mercury's exosphere (Wurz and Lammer, 2003; Killen et al., 2007; Mura et al., 2007; Wurz et al., 2010; Jones et al., 2020). Concerning hydrogen in Mercury's exosphere, H^+ ions that originate in the solar wind, and a fraction of ionized exospheric H atoms that are accelerated in Mercury's magnetosphere (Anderson et al., 2011) and backscattered to the surface will partly diffuse and via recombinative desorption degasing to the exosphere mainly as H_2 molecules (Hunten et al., 1988; Potter, 1995; Tucker et al., 2019), while another part will produce H_2O from reactions with OH groups on or within the H-saturated regolith grain interfaces. The grains are saturated with solar wind H, thus the H_2 recombination might happen in the grains as well, and the H_2 will diffuse out, since it is chemically less bound to the mineral than the H atom (Jones et al., 2020). Thus, H_2 formation competes with the production of OH and H_2O in the regolith. In experiments it is found that on the Moon only $\sim 2\,\%$ of the implanted H^+ is released as H_2 (Crandall et al., 2019). However, on the Moon the OH is only observed at higher latitudes, where the temperature is low enough. On Mercury's dayside the temperature is too high that this process becomes important, but close to the terminator the temperature is cooler where this might happen. Although the solar wind proton flux is higher at Mercury's orbit compared to the Moon at 1 AU, the planets magnetosphere protects large areas from solar wind precipitation, which may indicate that the H_2 formation in the surface is also a

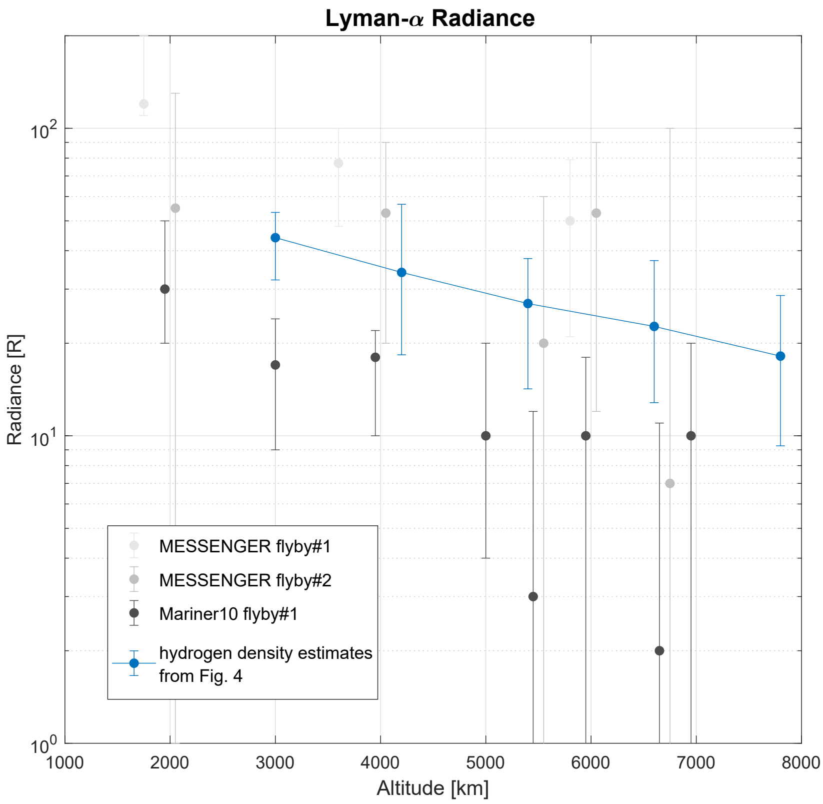

Figure 5. Airglow of hydrogen Lyman-α radiances around Mercury. The blue line shows the Lyman-α radiances obtained from the median (blue dot), upper and lower quartile (blue errorbar) of the hydrogen densities boxplot in Fig. 4. The gray and black dots show the Lyman-α observations of MESSENGER and Mariner 10 during their flybys (Vervack et al., 2011; Ishak, 2019).

not very efficient process (Hunten et al., 1988). Therefore, these studies suggested that photolysis of exospheric OH and H_2O molecules, stemming from the bombardment of micrometeoroids (Boradfoot et al., 1976; Hunten et al., 1988; Killen et al., 1997; Killen and Ip, 1999), may be a much more efficient source of H_2 near the surface than chemical reactions in the surface (Jones et al., 2020). Note that these micrometeoroids are smaller and more common in comparison to the large meteoroids, which might yield transient enhancements of the exosphere at high altitudes (Mangano et al., 2007; Jasinski et al., 2020).

One can estimate the H_2O density at Mercury's surface by using the estimated flux of $1 \times 10^8\,\mathrm{cm^{-2}s^{-1}}$ of H_2O from the vaporization of micrometeoroids (Killen et al., 1997). If we scale the H_2O photodissociation time for average solar activity at 1 AU (Huebner and Mukherjee, 2015) to Mercury's average orbital distance of 0.38 AU, we obtain $\sim 10^4$ s. The average micrometeorid related column density of H_2O is then $1 \times 10^{12}\,\mathrm{cm^{-2}}$. By using an average temperature of 4000 K for the ejecta gas/water vapor (Wurz and Lammer, 2003) one obtains a scale height for micrometeorid related H_2O vapor of ~ 500 km. This would yield a surface number density of $2 \times 10^4\,\mathrm{cm^{-3}}$. This value is lower than the upper limit of possible H_2O surface density of $1.5 \times 10^7\,\mathrm{cm^{-3}}$, estimated by earlier studies (Hunten et al., 1988). However, there will also be a thermal H_2O population on Mercury, that is produced by surface reactions and evaporation from ice deposits on the nightside or from the planet's interior (Hunten et al., 1988; Killen et al., 1997, 1997; Moses et al., 1999; Deutsch et al., 2019). H_2O molecules will be dissociated in H and OH and $\sim 13\,\%$ will yield H_2 and O atoms (Gombosi et al., 1986; Hunten et al., 1988). Photochemical reactions most likely enhance the lifetime of H_2O molecules near Mercury's surface by ~ 8 times (Hunten et al., 1988).

Moreover, a fraction of OH will be adsorbed at the surface where it also reacts with H so that H_2O can be recycled near the surface too. Previous studies showed that the number density of thermally released H_2O molecules decreases fast to negligible values above $1.3\,R_{\mathrm{M}}$. The hotter micrometeoroid-related H_2O population reaches $2\,R_{\mathrm{M}}$ with a number density of a few $\mathrm{cm^{-3}}$. Because of the decreasing availability of OH and O molecules at these distances, H atoms that will be produced via dissociation of H_2 molecules will not be efficiently removed by photochemical processes with these molecules. Although, H atoms (that are produced from H_2O molecules that originate from vaporized micrometeoroids) may contribute to the atomic H number densities, which we have inferred from the ICW observations upstream of the bow shock in the solar wind, we expect that the main source of our derived H number densities between $2 - 8\,R_{\mathrm{M}}$ is the dissociation of H_2 molecules.

The simulation output that reproduces the observationally derived H density at distances that are $> 1.5\,R_{\mathrm{M}}$ best, yields a H_2 surface density of $\sim 8 \times 10^4\,\mathrm{cm^{-3}}$. Such an H_2 surface density yields a modeled atomic H density of $100 - 10\,\mathrm{cm^{-3}}$ between $2 - 8\,R_{\mathrm{M}}$ (solid red line in Fig. 4) with an escape rate of dissociated H atoms of $\sim 6 \times 10^{25}\,\mathrm{s^{-1}}$. From our analysis, we can therefore constrain the so far unknown and overestimated H_2 surface number density to $\sim 8 \times 10^4\,\mathrm{cm^{-3}}$. This value allows us to study in the future the details of the solar wind implantation into Mercury's regolith that leads to H, H_2, OH, H_2O production and exospheric release as well as H_2O photochemistry in the exosphere. It will give us the opportunity to investigate and separate the H_2O sources and sinks on the innermost planet of the solar system. We expect that future measurements by the BepiColombo mission, in particular by the STROFIO and PICAM instruments of the SERENA package (Orsini et al., 2021a, 2021b), will help refine our knowledge about Mercury's exosphere.

Appendix A Exospheric H_2, H modeling

In this study we apply an exospheric Monte Carlo model that was successfully applied in previous studies related to Mercury's exosphere (Wurz and Lammer, 2003; Wurz et al., 2010; Pfleger et al., 2015). The Monte Carlo model assumes angular and velocity distributions at the surface in three dimensions as prescribed by a release process. Here we assume that the H_2 molecules are thermalized near the surface so that they result in a thermal distribution with a corresponding surface temperature of 638.74 K. The H_2 molecules follow individual trajectories through the exosphere until the molecules are ionized, dissociated, hit the surface or are lost from Mercury's gravity field. For integrating a system of ordinary equations for dissociation and ionization from the planetary surface up to 8 Mercury radii, we use the obtained loss rate L, that can also be expressed by a modified Jeans escape formula that is based on a shifted Maxwellian particle distribution

$$L = \sqrt{\frac{\mathrm{k_B} T_0}{2 m_{\mathrm{H_2}}}} \frac{N_0}{\sqrt{\pi}} F(u), \quad F(u) = \int_{\sqrt{\lambda}}^{\infty} \left[1 - (1 - 2uv) e^{2uv}\right] \frac{v}{u^2} e^{-v^2 - u^2} \, dv. \tag{A1}$$

Here, $\mathrm{k_B}$ is the Boltzmann constant, $m_{\mathrm{H_2}}$ the mass of molecular hydrogen and T_0 and N_0 are the surface temperature and density. $F(u)$ is the velocity distribution function, with u the mean velocity normalized to the local thermal speed $\sqrt{2\mathrm{k_B}\frac{T_0}{m_{\mathrm{H_2}}}}$, determined by solving $u = F(u)$. In the limit $u = 0$, the function $F(u)$ is reduced to $F(u) = (1 + \lambda)e^{-\lambda}$, which yields the usual Jeans escape formula with λ the Jeans parameter given by $(\mathrm{G} M m_{\mathrm{H_2}})/(\mathrm{k_B} T_0 R_{\mathrm{M}})$. Here, G is the gravitational constant and M and R_{M} are Mercury's mass and radius.

The H, H^+ and H_2^+ profiles were obtained after integrating the system of ordinary equations for ionization, dissociation and recombination, which can be written as

$$\begin{aligned}
\frac{1}{r^2} L \frac{\mathrm{d}s}{\mathrm{d}r} &= \alpha_2 \xi_{\mathrm{H_2^+}} \rho^2 (\xi_{\mathrm{H_2^+}} + 2\xi_{\mathrm{H^+}}) + \nu_{\mathrm{d}} (1 - s - \xi_{\mathrm{H_2^+}}) - 2\alpha_3 (s - \xi_{\mathrm{H^+}})^2 (s+1) \rho^3 \\
\frac{1}{r^2} L \frac{\mathrm{d}\xi_{\mathrm{H_2^+}}}{\mathrm{d}r} &= \nu_{\mathrm{i2}} \rho (1 - s - \xi_{\mathrm{H_2^+}}) - \alpha_2 \xi_{\mathrm{H_2^+}} (\xi_{\mathrm{H_2^+}} + 2\xi_{\mathrm{H^+}}) \rho^2 \\
\frac{1}{r^2} L \frac{\mathrm{d}\xi_{\mathrm{H^+}}}{\mathrm{d}r} &= \nu_{\mathrm{i1}} \rho (s - \xi_{\mathrm{H^+}}) - \alpha_1 \xi_{\mathrm{H^+}} (\xi_{\mathrm{H_2^+}} + 2\xi_{\mathrm{H^+}}) \rho^2
\end{aligned} \tag{A2}$$

Although, atom recombination has only a small influence in the results, in accordance to previous works (Yelle, 2004; Tian et al., 2008; Erkaev et al., 2016, 2017) the process is included and treated as a three body reaction $\mathrm{H} + \mathrm{H} + \mathrm{M} \rightarrow \mathrm{H_2} + \mathrm{M}$. Eqs. A2 were solved in normalized quantities and the distance r from the planetary center is normalized to R_p. L is normalized to $(N_0 m_{\mathrm{H_2}} V_{\mathrm{T_0}} R_p^2)$, where $V_{\mathrm{T_0}} = \sqrt{\mathrm{k_B} T_0 / m_{\mathrm{H}}}$, N_0 is the H_2 number density at the planetary surface. The total density ρ is normalized to $(N_0 m_{\mathrm{H_2}})$. The normalized rates with the normalization factor in brackets can be written as

$$\begin{aligned}
\nu_d &= 6.103 \cdot 10^{-7} (R_p / V_{\mathrm{T_0}}) \\
\nu_{i1} &= 8.623 \cdot 10^{-7} (R_p / V_{\mathrm{T_0}}) \\
\nu_{i2} &= 5.537 \cdot 10^{-7} (R_p / V_{\mathrm{T_0}}) \\
\alpha_1 &= 4 \cdot 10^{-12} (300/T_0)^{0.64} (N_0 R_p / V_{\mathrm{T_0}}) \\
\alpha_2 &= 2.3 \cdot 10^{-8} (300/T_0)^{0.4} (N_0 R_p / V_{\mathrm{T_0}}) \\
\alpha_3 &= 5.7 \cdot 10^{-32} (300/T_0)^{1.6} (2 N_0^2 R_p / V_{\mathrm{T_0}})
\end{aligned} \tag{A3}$$

Here, ρ is the total mass density, s is the ratio of the atomic $(\mathrm{H}+\mathrm{H}^+)$ and total mass density, ξ_{H^+}, $\xi_{\mathrm{H}_2^+}$ are the mass fractions of the atomic (H^+) and molecular (H_2^+) ions, α_1, α_2 and α_3 are the coefficients of recombination ($\mathrm{H}^+ + \mathrm{e}^- \rightarrow \mathrm{H}$), ($\mathrm{H}_2^+ + \mathrm{e}^- \rightarrow \mathrm{H}_2$) and ($\mathrm{H}+\mathrm{H} \rightarrow \mathrm{H}_2$), respectively, and $\nu_{\mathrm{i}1}$, $\nu_{\mathrm{i}2}$ and ν_{d} are rates of photoionization of H, H_2 and dissociation, respectively. Note that the ionization and dissociation rates of H and H_2 correspond to the average values over all 2247 ICW events. The H_2 photoionization and dissociation rates were calculated for each event seperately according to the Flare Irradiance Spectral Model (FISM-P, (chamberlain et al., 2008)) and radial distance from Mercury to the Sun during the event observation (see also section: Hydrogen density estimate from ICW observation), and that the recombination coefficients are taken from previous publications (Johnstone et al., 2015; Yelle, 2004).

From the studied hydrogen-bearing species, molecular hydrogen is considered to be the major constituent and thus the total mass density is assumed to be approximately equal to that of the H_2 density.

We further determine the density ρ-function by interpolating the H_2 profile from Monte Carlo simulation H_2 results. Using the determined loss rate L and density ρ, we integrate the system of Eqs. A2 with respect to quantities ξ_{H^+} , $\xi_{\mathrm{H}_2^+}$ and s, which finally yields the radial distributions of the dissociated atomic hydrogen and ionized particles.

Acknowledgments

DS like to thank M. Delva for fruitful discussions on pick-up ion cyclotron waves and acknowledge the support from the Austrian Research Promotion Agency (FFG) ASAP MERMAG-4 under contract 865967.

Author contributions DS initiated this study, did the analysis, and wrote the paper. HL gave the initial idea of the exospheric model, used to explain the observationally derived results for constraining Mercruy's molecular hydrogen surface density, and contributed to writing and editing the manuscript. FP and MV contributed to the analysis, the interpretation of the results, and helped editing the paper. NVE and AV set up the simulations and contributed the simulation results. WB, YN and PW gave valuable input to the manuscript and helped evaluating the paper. BJA guaranteed the quality of magnetic field data of MESSENGER.

Data availability The magnetic field (MAG) data from the MESSENGER spacecraft are public available at the NASA Planetary Data System (PDS) and can be retrieved on their website (`https://pds-ppi.igpp.ucla.edu/search/view/?f=yes&id=pds://PPI/MESS-E_V_H_SW-MAG-4-SUMM-CALIBRATED-V1.0/DATA/MSO`).

The numerical results in Fig. 4 are produced by the model described in Appendix A.

The solar wind density and velocity data were obtained from the AMDA database (`http://amda.cdpp.eu/`). All data are open-access and can be downloaded on their website via the Workspace Explorer under: Solar Wind Propagation Models/Mercury/Tao Model/SW/Input OMNI.

The orbital motion of Mercury were retrieved from the Navigation and Ancillary Information Facility (NAIF), publicly accessible on the NASA Jet Propulsion Laboratory (JPL) webpage (`https://wgc.jpl.nasa.gov:8443/webgeocalc/#StateVector`).

The solar spectral irradiance to determine the solar acitvity during the event obsevations were obtained from the Flare Irradiance Spectral Model for Mercruy (FISM-P, (chamberlain et al., 2008)), provided by the LASP Interactive Solar iRradiance Data-center (LISIRD), publicly accessible on their webpage (`https://lasp.colorado.edu/lisird/data/fism_p_ssi_mercury/`).

References

B. J. Anderson, M. H. Acuña, D. Lohr, J. Scheifele, A. Raval, H. Korth, and J. Slavin. The Magnetometer Instrument on MESSENGER. *Space Sci. Rev.*, 131:417–450, 2007.

B. J. Anderson, C. L. Johnson, H. Korth, M. E. Purucker, R. M. Winslow, J. A. Slavin, S. C. Solomon, R. L. McNutt, J. M. Raines, and T. H. Zurbuchen. The Global Magnetic Field of Mercury from MESSENGER Orbital Observations. *Science*, 333(6051):1859–1862, 2011.

C. H. Acton. Ancillary data services of NASA's Navigation and Ancillary Information Facility. *Planet. Space Sci.*, 44(1):65–70, 1996.

C. W. Arthur, R. L. McPherron, and J. D. Means. A comparative study of three techniques for using the spectral matrix in wave analysis. *Radio Science*, 11(10):833–845, 1976.

J. Bishop and J. W. Chamberlain. Radiation pressure dynamics in planetary exospheres: A "natural" framework. *Icarus*, 81(1"):145–163, 1989.

A. L. Broadfoot, S. Kumar, M. J. S. Belton, and M. B. McElroy. Mercury's Atmosphere from Mariner 10: Preliminary Results. *Science*, 185(4146):166–169, 1974.

A. L. Broadfoot, D. E. Shemansky, and S. Kumar. Mariner 10: Mercury atmosphere. *Geophys. Res. Lett.*, 3(10):577–580, 1976.

M. H. Burger, R. M. Killen, W. E. McClintock, A. W. Merkel, R. J. Vervack, T. A. Cassidy, and M. Sarantos. Seasonal variations in Mercruy's dayside calcium exosphere. *Icarus*, 238:51–58, 2014.

T. A. Cassidy, A. W. Merkel, M. H. Burger, M. Sarantos, R. M. Killen, W. E. McClintock, and R. J. Vervack. Mercury's seasonal sodium exosphere: MESSENGER orbital observations. *Icarus*, 248:547–559, 2015.

J. W. Chamberlain. Planetary coronae and atmospheric evaporation. *Planet. Space Sci.*, 11(8):901–960, 1963.

J. W. Chamberlain, D. M. Hunten. Theory of Planetary Atmospheres, 2nd ed. *New York: Academic Press*, Chapter 6:292, 1987.

P. C. Chamberlin, T. N. Woods, and F. G. Eparvier. Flare Irradiance Spectral Model (FISM): Flare component algorithms and results. *Space Weather*, 6:1542–7390, 2008.

A. A. Christou, R. M. Killen, and M. H. Burger. The meteoroid stream of comet Encke at Mercury: Implications for MErcury Surface, Space ENvironment, GEochemistry, and Ranging observations of the exosphere. *Geophys. Res. Lett.*, 42: 7311—7318, 2015.

P. B. Crandall, J. J. Gillis-Davis, and R. I. Kaiser. Untangling the origin of molecular hydrogen in the lunar exosphere. *Astrophys. J.*, 887:27, (7pp), 2019.

M. M. Cowee, S. P. Gary, and H. Y. Wei. Pickup ions and ion cyclotron wave amplitudes upstream of Mars: First results from the 1D hybrid simulation. *Geophys. Res. Lett.*, 39(8), 2012.

M. M. Cowee, D. Winske, C. T. Russell, and R. J. Strangeway. 1D hybrid simulations of planetary ion-pickup: Energy partition. *Geophys. Res. Lett.*, 34(2), 2007.

M. Delva, C. Mazelle, and C. Bertucci. Upstream Ion Cyclotron Waves at Venus and Mars. *Space Sci. Rev.*, 162:25–24, 2011.

M. Delva, M. Volwerk, C. Mazelle, J. Y. Chaufray, J. L. Bertaux, T. L. Zhang, and Z. Vörös. Hydrogen in the extended Venus exosphere. *Geophys. Res. Lett.*, 36(1), 2009.

M. Delva, T. L. Zhang, M. Volwerk, Z. Vörš, and S. A. Pope. Proton cyclotron waves in the solar wind at Venus. *J. Geophys. Res: Planets*, 113(E9), 2008.

A. N. Deutsch, J. W. Head, and G. Neumann. Age constraints of Mercury's polar deposits suggest recent delivery of ice. *Earth and Planet. Sci. Lett.*, 520:26–33, 2019.

N. V. Erkaev, H. Lammer, P. Odert, K. G. Kislyakova, C. P. Johnstone, M. Güdel, and M. L. Khodachenko. EUV-driven mass-loss of protoplanetary cores with hydrogen-dominated atmospheres: the influences of ionization and orbital distance. *MNRAS*, 460(2):1300–1309, 2016.

N. V. Erkaev, P. Odert, H. Lammer, K. G. Kislyakova, L. Fossati, A. V. Mezentsev, C. P. Johnstone, D. I. Kubyshkina, I. F. Shaikhislamov, and M. L. Khodachenko. Effect of stellar wind induced magnetic fields on planetary obstacles of non-magnetized hot Jupiters. *MNRAS*, 470(4):4330–4336, 2017.

W. Exner, S. Simon, D. Heyner, and U. Motschmann. Influence of Mercury's Exosphere on the Structure of the Magnetosphere. *J. Geophys. Res: Space Physics*, 125(7):e2019JA027691, 2020.

R. A. Fowler, B. J. Kotick, and R. D. Elliott. Polarization analysis of natural and artificially induced geomagnetic micropulsations. *J. Geophys. Res: Space Physics*, 72(11):2871–2883, 1967.

S. P. Gary. Electromagnetic Ion / Ion Instabilities and Their Consequences in Space Plasmas - a Review. *Space Sci. Rev.*, 56(3-4):373–415, may 1991.

T. I. Gombosi, A. F. Nagy, and T. E. Cravens. Dust and neutral gas modeling of the inner atmospheres of comets. *Reviews of Geophysics*, 24:667–700, 1986.

D. E. Huddleston and A. D. Johnstone. Relationship between wave energy and free energy from pickup ions in the comet Halley environment. *J. Geophys. Res: Space Physics*, 97(A8):12217–12230, 1992.

W. F. Huebner and J. Mukherjee. Photoionization and photodissociation rates in solar and black body radiation fields. *Planet. Space Sci.*, 106:11–45, 2015.

D. M. Hunten, T. H. Morgan, and D. E. Shemansky. *The Mercury atmosphere*, pages 562–612, 1988.

B. Ishak. Mercury: the view after MESSENGER. *Contemporary Physics*, 60(4):341–341, 2019.

M. K. James, S. M. Imber, E. J. Bunce, T. K. Yeoman, M. Lockwood, M. J. Owens, and J. A. Slavin. Interplanetary magnetic field properties and variability near Mercury's orbit. *J. Geophys. Res: Space Physics*, 122: 7907–7924, 2017.

J. M. Jasinski, L. H. Regoli, T. A. Cassidy, R. M. Dewey, J. M. Raines, J. A. Slavin, A. J. Coates, D. J. Gershman, T. A. Nordheim, and N. Murphyand. A transient enhancement of Mercury's exosphere at extremely high altitudes inferred from pickup ions. *Nat. Commun.*, 11: 4350, 2020.

C. P. Johnstone, M. Güdel, A. Stökl, H. Lammer, L. Tu, K. G. Kislyakova, T. Lüftinger, P. Odert, N. V. Erkaev, and E. A. Dorfi. The Evolution of Stellar Rotation and the Hydrogen Atmospheres of Habitable-zone Terrestrial Planets. *Astrophys. J. Lett.*, 815(1):L12, 2015.

B. M. Jones, M. Sarantos, and T. M. Orlando. A New In Situ Quasi-continuous Solar-wind Source of Molecular Water on Mercury. *The Astrophysical Journal*, 891(2):L43, 2020.

R. Killen, G. Cremonese, H. Lammer, S. Orsini, A. E. Potter, A. L. Sprague, P. Wurz, M. L. Khodachenko, H. I. M. Lichtenegger, A. Milillo, and Mura. Processes that Promote and Deplete the Exosphere of Mercury. *Space Sci. Rev.*, 132(2-4):433–509, 2007.

R. Killen, D. Shemansky, and N. Mouawad. Expected Emission from Mercury's Exospheric Species, and their Ultraviolet-Visible Signatures. *The Astrophysical Journal Supplement Series*, 181(2):351–359, 2009.

R. M. Killen, J. Benkhoff, and T. H. Morgan. Mercury's Polar Caps and the Generation of an OH Exosphere. *Icarus*, 125(1):195–211, 1997.

R. M. Killen and W.-H. Ip. The surface-bounded atmospheres of Mercury and the Moon. *Reviews of Geophysics*, 37(3):361–406, 1999.

S. Kumar. Mercury's Atmosphere: A Perspective after Mariner 10. *Ikarus*, 28(4):579–591, 1976.

V. Mangano, A. Milillo, A. Mura, S. Orsini, E. DeAngelis, A.M. DiLellis, and P. Wurz. The contribution of impact-generated vapour to the hermean atmosphere. *Planet. Space Sci.*, 55(11):1541–1556, 2007.

C. Mazelle and F. M. Neubauer. Discrete wave packets at the proton cyclotron frequency at comet P/Halley. *Geophys. Res. Lett.*, 20(2):153–156, 1993.

C. Mazelle, D. Winterhalter, K. Sauer, J. G. Trotignon, M. H. Acuña, K. Baumgärtel, C. Bertucci, D. A. Brain, S. H. Brecht, M. Delva, E. Dubinin, M. Øieroset, and J. Slavin. Bow Shock and Upstream Phenomena at Mars. *Space Sci. Rev.*, 111(1):115–181, 2004.

W. E. McClintock and M. R. Lankton. The Mercury Atmospheric and Surface Composition Spectrometer for the MESSENGER Mission. *Space Sci. Rev.*, 131(1-4):481–521, 2007.

J. D. Means. Use of the three-dimensional covariance matrix in analyzing the polarization properties of plane waves. *J. Geophys. Res: Space Physics*, 77(28):5551–5559, 1972.

A. W. Merkel, T. A. Cassidy, R. J. Vervack, W. E. McClintock, M. Sarantos, M. H. Burger, and R. M. Killen. Seasonal variations of Mercury's magnesium dayside exosphere from MESSENGER observations. *Icarus*, 281:46–54, 2017.

J. I. Moses, K. Rawlins, K. Zahnle, and L. Dones. External Sources of Water for Mercury's Putative Ice Deposits. *Icarus*, 137(2):197–221, 1999.

A. Mura, A. Milillo, S. Orsini, and S. Massetti. Numerical and analytical model of Mercury's exosphere: Dependence on surface and external conditions. *Planet. Space Sci.*, 55(11):1569–1583, 2007.

S. Orsini, S. A. Livia, H. Lichtenegger, S. Barabasha, A. Milillo, E. De Angelis, M. Phillips, G. Laky, M. Wieser, A. Olivieri, C. Plainaki, G. Ho, R.M. Killen, J.A. Slavin, P. Wurz, J.-J. Berthelier, I. Dandouras, E. Kallio, S. McKenna-Lawlor, S. Szalai, K. Torkar, O. Vaisberg, F. Allegrini, I.A. Daglis, C. Dong, C.P. Escoubet, S. Fatemi, M. Fränz, S. Ivanovski, N. Krupp, H. Lammer, F. Leblanc, V. Mangano, A. Mura, H. Nilsson, J.M. Raines, R. Rispoli, M. Sarantos, H.T. Smith, K. Szego, A. Aronica, F. Camozzi, A.M. Di Lellis, G. Fremuth, F. Giner, R. Gurnee, J. Hayes, H. Jeszenszky, F. Tominetti, B. Trantham, J. Balaz, W. Baumjohann, D. Brienza, U. Bührke, M.D. Bush, M. Cantatore, S. Cibella, L. Colasanti, G. Cremonese, L. Cremonesi, M. D'Alessandro, D. Delcourt, M. Delva, M. Desai, M. Fama, M. Ferris, H. Fischer, A. Gaggero, D. Gamborino, P. Garnier, W.C. Gibson, R. Goldstein, M. Grande, V. Grishin, D. Haggerty, M. Holmström, I. Horvath, K.-C. Hsieh, A. Jacques, R.E. Johnson, A. Kazakov, K. Kecskemety, H. Krüger, C. Kürbisch, F. Lazzarotto, F. Leblanc, M. Leichtfried, R. Leoni, A. Loose, D. Maschietti, S. Massetti, F. Mattioli, G. Miller, D. Moissenko, A. Morbidini, R. Noschese, F. Nuccilli, C. Nunez, N. Paschalidis, S. Persyn, D. Piazza, M. Oja, J. Ryno, W. Schmidt, J.A. Scheer, A. Shestakov, S. Shuvalov, K. Seki, S. Selci, K. Smith, R. Sordini, J. Svensson, L. Szalai, D. Toublanc, C. Urdiales, A. Varsani, N. Vertolli, R. Wallner, P. Wahlstroem, P. Wilson, and S. Zampieri. SERENA: Particle Instrument Suite for Determining the Sun-Mercury Interaction from BepiColombo. *Space Sci. Rev.*, 217, 2021.

S. Orsini, S.A. Livia, H. Lichtenegger, S. Barabasha, A. Milillo, E. De Angelis, M. Phillips, G. Laky, M. Wieser, A. Olivieri, C. Plainaki, G. Ho, R.M. Killen, J.A. Slavin, P. Wurz, J.-J. Berthelier, I. Dandouras, E. Kallio, S. McKenna-Lawlor, S. Szalai, K. Torkar, O. Vaisberg, F. Allegrini, I.A. Daglis, C. Dong, C.P. Escoubet, S. Fatemi, M. Fränz, S. Ivanovski, N. Krupp, H. Lammer, F. Leblanc, V. Mangano, A. Mura, H. Nilsson, J.M. Raines, R. Rispoli, M. Sarantos, H.T.

Smith, K. Szego, A. Aronica, F. Camozzi, A.M. Di Lellis, G. Fremuth, F. Giner, R. Gurnee, J. Hayes, H. Jeszenszky, F. Tominetti, B. Trantham, J. Balaz, W. Baumjohann, D. Brienza, U. Bührke, M.D. Bush, M. Cantatore, S. Cibella, L. Colasanti, G. Cremonese, L. Cremonesi, M. D'Alessandro, D. Delcourt, M. Delva, M. Desai, M. Fama, M. Ferris, H. Fischer, A. Gaggero, D. Gamborino, P. Garnier, W.C. Gibson, R. Goldstein, M. Grande, V. Grishin, D. Haggerty, M. Holmström, I. Horvath, K.-C. Hsieh, A. Jacques, R.E. Johnson, A. Kazakov, K. Kecskemety, H. Krüger, C. Kürbisch, F. Lazzarotto, F. Leblanc, M. Leichtfried, R. Leoni, A. Loose, D. Maschietti, S. Massetti, F. Mattioli, G. Miller, D. Moissenko, A. Morbidini, R. Noschese, F. Nuccilli, C. Nunez, N. Paschalidis, S. Persyn, D. Piazza, M. Oja, J. Ryno, W. Schmidt, J.A. Scheer, A. Shestakov, S. Shuvalov, K. Seki, S. Selci, K. Smith, R. Sordini, J. Svensson, L. Szalai, D. Toublanc, C. Urdiales, A. Varsani, N. Vertolli, R. Wallner, P. Wahlstroem, P. Wilson, and S. Zampieri. Correction to: SERENA: Particle Instrument Suite for Determining the Sun-Mercury Interaction from BepiColombo. *Space Sci. Rev.*, 217, 2021.

L. C. Philpott, C. L. Johnson, B. J. Anderson, and R. M. Winslow. The Shape of Mercury's Magnetopause: The Picture From MESSENGER Magnetometer Observations and Future Prospects for BepiColombo. *J. Geophys. Res: Space Physics*, 125(5):1569–1583, 2020.

M. Pfleger, H. I. M. Lichtenegger, P. Wurz, H. Lammer, E. Kallio, M. Alho, A. Mura, S. McKenna-Lawlor, J. A. Martin-Fernandez. 3D-modeling of Mercury's solar wind sputtered surface-exosphere environment. *Planet. Space Sci.*, 115:90–101, 2015.

P. Pokorný, M. Sarantos, and D. Janches. A Comprehensive Model of the Meteoroid Environment around Mercury. *The Astrophysical Journal*, 863(1), 2018.

A. E. Potter. Chemical sputtering could produce sodium vapor and ice on Mercury. *Geophys. Res. Lett.*, 22(23):3289–3292, 1995.

C. Russell, S. Mayerberger, and X. Blanco-Cano. Proton cyclotron waves at Mars and Venus. *Advances in Space Research*, 38(4):745–751, 2006.

J. C. Samson and J. V. Olson. Some comments on the descriptions of the polarization states of waves. *Geophysical Journal International*, 61(1):115–129, 04 1980.

D. Schmid, Y. Narita, F. Plaschke, M. Volwerk, R. Nakamura, and W. Baumjohann. Pick-Up Ion Cyclotron Waves Around Mercury. *Geophys. Res. Lett.*, 48(9):0094–8276, 2021.

J. A. Slavin and R. E. Holzer. Solar wind flow about the terrestrial planets, 1. Modeling bow shock position and shape. *J. Geophys. Res: Space Physics*, 86(A13):11401–11418, 1981.

S. C. Solomon, R. L. McNutt, R. E. Gold, and D. L. Domingue. MESSENGER Mission Overview. *Space Sci. Rev.*, 131:3–39, 2007.

C. Tao, R. Kataoka, H. Fukunishi, Y. Takahashi, and T. Yokoyama. Magnetic field variations in the jovian magnetotail induced by solar wind dynamic pressure enhancements. *J. Geophys. Res: Space Physics*, 110(A11), 2005.

F. Tian, J. F. Kasting, H.-L. Liu, R. G. Roble. Hydrodynamic planetary thermosphere model: 1. Response of the Earth's thermosphere to extreme solar EUV conditions and the significance of adiabatic cooling. *J. Geophys. Res.*, 113(E5), 2008.

O. J. Tucker, W. M. Farrell, R. M. Killen, and D. M. Hurley. Solar Wind Implantation Into the Lunar Regolith: Monte Carlo Simulations of H Retention in a Surface With Defects and the H_2 Exosphere. *J. Geophys. Res: Planets*, 124(2):278–293, 2019.

R. J. Vervack, R. M. Killen, A. L. Sprague, M. H. Burger, A. W. Merkel, and M. Sarantos. Early MESSENGER Results for Less Abundant or Weakly Emitting Species in Mercury's Exosphere. In *EPSC-DPS Joint Meeting 2011*, volume

2011, page 1131, 2011.
R. J. Vervack, W. E. McClintock, E. T. Bradley, R. M. Killen, A. L. Sprague, N. Mouawad, N. R. Izenberg, M. C. Kochte, and M. R. Lankton. MESSENGER Observations of Mercury's Exosphere: Discoveries and Surprises from the First Two Flybys. In *Lunar and Planetary Science Conference*, Lunar and Planetary Science Conference, page 2220, 2009.
R. J. Vervack, W. E. McClintock, R. M. Killen, A. L. Sprague, B. J. Anderson, M. H. Burger, E. T. Bradley, N. Mouawad, S. C. Solomon, and N. R. Izenberg. Mercury's Complex Exosphere: Results from MESSENGER's Third Flyby. *Science*, 329(5992):672–675, 2010.
R. J. Vervack Jr., R. M. Killen, W. E. McClintock, A. W. Merkel, M. H. Burger, T. A. Cassidy, and M. Sarantos. New discoveries from MESSENGER and insights into Mercury's exosphere. *Geophys. Res. Lett.*, 43(22):11,545–11,551, 2016.
R. M. Winslow, B. Anderson, C. Johnson, J. Slavin, H. Korth, M. Purucker, D. N. Baker, and S. Solomon. Mercury's magnetopause and bow shock from MESSENGER Magnetometer observations. *J. Geophys. Res: Space Physics*, 118:2213–2227, 2013.
C. S. Wu and R. C. Davidson. Electromagnetic instabilities produced by neutral-particle ionization in interplanetary space. *J. Geophys. Res: Space Physics*, 77(28):5399–5406, 1972.
C. S. Wu, R. E. Hartle, and K. W. Ogilvie. Interaction of singly charged interstellar helium ions with the solar wind. *J. Geophys. Res: Space Physics*, 78(1):306–309, 1973.
P. Wurz, D. Gamborino, A. Vorburger, and J. M. Raines. Heavy Ion Composition of Mercury's Magnetosphere. *J. Geophys. Res: Space Physics*, 124(4):2603–2612, 2019.
P. Wurz and H. Lammer. Monte-Carlo simulation of Mercury's exosphere. *Icarus*, 164(1):1–13, 2003.
P. Wurz, J. A. Whitby, U. Rohner, J. A. Martin-Fernandez, H. Lammer, and C. Kolb. Self-consistent modelling of Mercury's exosphere by sputtering, micro-meteorite impact and photon-stimulated desorption. *Planetary and Space Science*, 58(12):1599–1616, 2010.
R. V. Yelle. Aeronomy of extra-solar giant planets at small orbital distances. *Ikarus*, 170(1):167–179, 2004.